2024 IEEE/RSJ International Conference on Intelligent Robots and Systems (IROS)
October 14-18, 2024. Abu Dhabi, UAE

Visual Servo Control of a Conceptual Magnetically Anchored and Guided Flexible Endoscope

Weibing Li, Yang Yang and Yongping Pan

Abstract— **This paper presents a conceptual magnetically anchored and guided flexible endoscope for minimally invasive surgery (MIS). Leveraging both the magnetic coupling between the external and internal permanent magnets and the bending of a flexible joint, the endoscope offers improved maneuverability and adaptability within confined surgical spaces. The visual servo control allows the endoscope to autonomously track surgical instruments during procedures, thereby reducing the risk of human error and operator fatigue. First, the design and working principles of the endoscope are introduced. Subsequently, the kinematic modeling of the endoscope is derived, and the control scheme is developed based on a quadratic programming (QP) framework by taking into account both magnetically anchoring constraints and physical constraints, where the joint velocities can be resolved given the desired task velocities in a one-step way. Simulative validations are conducted to verify the effectiveness of the visual servo control for the presented endoscope tracking a static/dynamic target with physical constraints considered.**

I. INTRODUCTION

In recent years, minimally invasive surgery (MIS) has developed rapidly due to its benefits such as reduced pain, quicker return of oral intake, shorter hospitalizations, and improved cosmetic results compared to traditional open surgery [1]. To further enhance cosmetic benefits and reduce morbidity of MIS, single-port access (SPA) surgery requiring a single incision has been introduced [2]. In SPA surgery, the endoscope and several surgical instruments enter the human body via a single portal, where the space is congested due to the passage and occupation of the surgical instruments and endoscope. The congestion will potentially lead to the fencing between the surgical instruments and the endoscope, as well as restricted camera views of the endoscope.

To alleviate the problem, a method is to use the magnetically anchored and guided system (MAGS) endoscope. Unlike the conventional endoscope with a rigid shaft, a MAGS endoscope can be inserted into the body of the patient and be anchored against the abdominal wall via a magnetic coupling between the external permanent magnet (EPM) and internal permanent magnet (IPM). The endoscope can be anchored at a distance from the port to reduce the space it occupies, which can ease congestion within the port. This allows the surgeon more freedom to maneuver surgical instruments and enhances the camera views provided by the endoscope. The early MAGS endoscopes [3], [4], [5], were manually operated by the assistant, making them difficult to control and potentially leading to muscle fatigue. This could result in miscommunication between the assistant's actions and the surgeon's commands. In [6], a soft-bodied MAGS endoscope was presented, which utilized an EPM and two EPMs to establish two sets of magnetic couplings to provide the anchoring forces against gravity and bending forces to deflect a ball hinge, thereby altering the camera's pose. In [7], a MAGS endoscope was presented by leveraging the magnetic coupling formed by two sets of radially magnetized external and internal permanent magnets to achieve both translational and rotational movements of the camera.

In addition to MAGS endoscopes, flexible endoscopes have gained significant attention as an alternative to conventional rigid endoscopes, owing to their high versatility and maneuverability. Flexible endoscopes utilize flexible and steerable sections, acting as flexible joints, to control the pose of the endoscope. This design allows for a larger working space and a smaller operating space. In [8], a new class of thin, dexterous continuum robots leveraging the translations and rotations of telescoping, concentric, pre-bending superelastic tubes was presented, where the bending of the flexible joint is achieved by the elastic interaction in the backbone itself. In [9], a novel constrained wire-driven flexible endoscope was presented by employing an active constraint to control the length of the bending section and pulling the wires to control the curvature of the bending section. In [10], a novel flexible manipulator with ball-constrained spherical joints and a spring was proposed to improve the rigidity and accuracy of flexible robots. In [11], a flexible endoscope consisting of a UR5 robot with constrained tendon-driven continuum mechanism was presented to ensure improved flexibility and dexterity by introducing a constraint tube to control the angulation of the length of the flexible endoscope. Despite the improved flexibility and maneuverability, existing flexible endoscopes still require passage through a single-port access, inevitably occupying some port space.

In this paper, a conceptual magnetically anchored and guided flexible endoscope is presented, which integrates features from both the MAGS endoscope and flexible endoscope. This hybrid design enhances the flexibility and

*This work was supported in part by the National Natural Science Foundation of China under Grant 62206317, in part by the Guangdong Basic and Applied Basic Research Foundation under Grant 2022A1515012186, in part by the Young Talent Support Project of Guangzhou Association for Science and Technology under Grant QT-2023-018, and in part by the Guangzhou Haizhu District Science and Technology Program under Grant 2022-50. *(Corresponding author: Weibing Li.)*

Weibing Li and Yang Yang are with the School of Computer Science and Engineering, Sun Yat-sen University, Guangzhou 510006, China (e-mail: liwb53@mail.sysu.edu.cn; yangy787@mail2.sysu.edu.cn.)

Yongping Pan is with the School of Advanced Manufacturing, Sun Yat-sen University, Shenzhen 518107, China (e-mail: panyongp@mail.sysu.edu.cn).

maneuverability of the MAGS endoscope while reducing the port pace that conventional flexible endoscopes inevitably occupy. Contributions of this paper include the following: First, the design and working principle of a conceptual magnetically anchored and guided flexible endoscope is presented. Second, the kinematic modeling is derived and the control scheme is developed based on a quadratic programming (QP) framework by introducing the magnetically anchoring constraints as equality constraints, where the joint velocities can be resolved given the desired task velocities in a one-step way. Last, simulative validations verify the feasibility of visual servo for the presented endoscope tracking a static/dynamic target with physical constraints considered.

The remainder of this paper is organized as follows. In Section II, the design and working principle of the presented conceptual endoscope is detailed. Sections III and IV present the kinematic modeling and control scheme of the endoscope, respectively. Simulative validations are conducted in Section V. Section VI concludes final remarks on this work.

II. DESIGN AND WORKING PRINCIPLE

This section details the design overview and the working principle of the presented endoscope system.

A. Design Overview

The MAGS flexible endoscope system, as depicted in Fig. 1(a), comprises two components: an external robot controller and a MAGS flexible endoscope.

The section view of the bending endoscope is demonstrated in Fig. 1(b). Outside the body cavity wall, the external robot controller comprises a Franka Emika Panda robot manipulator with an EPM attached as its end effector. Within the body cavity wall, the endoscope consists of an actuation module, a flexible joint, a holder, and a camera. At the top of the actuation module is an EPM. Two motors housed within the actuation module are connected to separate capstans. The flexible joint, made of flexible materials with holes around its circumference, is affixed to the end of the actuation module and secures a holder that accommodates the camera. Two groups of wires are wound around the two capstans and pass through the holes in the flexible joint.

B. Working Principle

The endoscope is inserted into the patient's body cavity through the incision. Once magnetically anchored on the body cavity wall, the magnetic coupling counteracts gravity, pulling the endoscope away from the incision. Assuming the cavity wall is approximately planar and the relative pose of the EPM and IPM remains constant, manipulating the robot manipulator changes the EPM's pose, thereby altering the IPM's pose. This guides the endoscope to slide along the body cavity wall, involving two translational movements within the plane and a rotational movement perpendicular to the plane. Additionally, by actuating the two motors inside the actuation module, the connected capstans spin to tension or slacken the wires. The force applied to the wires causes the flexible joint to bend along a specific direction, resulting in changes to the camera's pose.

III. KINEMATIC MODELING

The magnetically anchored and guided flexible endoscope system presented in this study offers a total of nine degrees of freedom (DoFs). Among these, seven are provided by the Franka Emika Panda robot, while the remaining two are facilitated by the flexible joint. When the endoscope is anchored on the body cavity wall, it is constrained to deliver five DoFs: two translational DoFs in the plane, a rotational DoF around the normal plane, a bending direction DoF, and a bending angle DoF. This section presents the kinematic modeling considering both magnetically anchoring contraints and physical constraints. The kinematic modeling encompasses mappings between joint space, task space, and image space.

A. Mapping Between Joint Space and Task Space

For the Franka Emika Panda robot, the associated transformation matrices from frame 0 to frame 7 can be prescribed as follows [12]:

$$ {}^{i-1}\boldsymbol{T}_i = \begin{bmatrix} c_{\theta_i} & -s_{\theta_i}c_{\alpha_i} & s_{\theta_i}s_{\alpha_i} & d_i c_{\theta_i} \\ s_{\theta_i} & c_{\theta_i}c_{\alpha_i} & -c_{\theta_i}s_{\alpha_i} & d_i s_{\theta_i} \\ 0 & s_{\alpha_i} & c_{\alpha_i} & l_i \\ 0 & 0 & 0 & 1 \end{bmatrix} \tag{1} $$

where i is the index of the ith actuator for $i = 1, 2, ..., 7$, $s_{\theta_i} = \sin(\theta_i)$, $c_{\theta_i} = \cos(\theta_i)$, $s_{\alpha_i} = \sin(\alpha_i)$, $c_{\alpha_i} = \cos(\alpha_i)$, and d_i, l_i, θ_i, α_i are Denavit-Hartenberg (DH) parameters. Naturally, the kinematics of the Franka Emika Panda robot can be computed as

$$ {}^0\boldsymbol{T}_7 = {}^0\boldsymbol{T}_1 {}^1\boldsymbol{T}_2 {}^2\boldsymbol{T}_3 {}^3\boldsymbol{T}_4 {}^4\boldsymbol{T}_5 {}^5\boldsymbol{T}_6 {}^6\boldsymbol{T}_7. \tag{2} $$

By differentiating equation (2), the Jacobian matrix of the robot is derived as follows:

$$ {}^0\boldsymbol{\xi}_{\text{robot}} = {}^0\boldsymbol{J}_{\text{robot}}\dot{\boldsymbol{\theta}}_{\text{robot}}, \tag{3} $$

where ${}^0\boldsymbol{\xi}_{\text{robot}}$ denotes the linear and angular velocities of the EMP in the base frame 0, $\dot{\boldsymbol{\theta}}_{\text{robot}}$ denotes the the joint velocities of the robot, ${}^0\boldsymbol{J}_{\text{robot}}$ is the Jacobian matrix of the robot in the base coordinate frame which maps from joint space to Cartesian space.

Note that the actuation module is anchored on the body cavity wall via magnetic coupling between the EPM and IPM. It is assumed that the relative pose between the EPM and IPM remains constant. Coordinate frames 7–10 assigned to the flexible robotic endoscope are illustrated in Fig. 1(b). Coordinate frame 7 is attached to the center of the EPM, while coordinate frame 8 is attached to the center of the actuation module. The transformation matrix between frame 7 and frame 8 is given as follows:

$$ {}^7\boldsymbol{T}_8 = \begin{bmatrix} 1 & 0 & 0 & 0 \\ 0 & 1 & 0 & d_{\text{offset}} \\ 0 & 0 & 1 & 0 \\ 0 & 0 & 0 & 1 \end{bmatrix}, \tag{4} $$

where d_{offset} denotes the distance between the EPM and the center of the actuation module. Coordinate frame 9 is attached to the distal end of the flexible joint. Coordinate

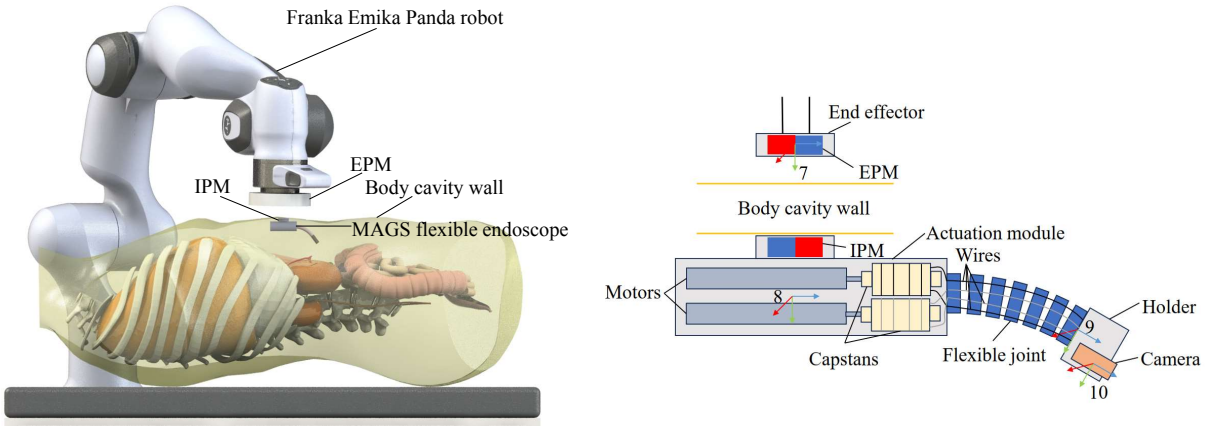

(a) (b)

Fig. 1. Design of the conceptual MAGS flexible endoscope system. (a) The MAGS flexible endoscope system. (b) Section view of the bending MAGS flexible endoscope.

frames 8 and 9 are linked by the following transformation matrix [11], [13]:

$$
{}^{8}\boldsymbol{T}_{9} = \begin{bmatrix} s_\alpha^2 + c_\alpha^2 c_\theta & c_\alpha s_\alpha \left(c_\theta - 1\right) & c_\alpha s_\theta & c_\alpha \left(1 - c_\theta\right) L/\theta \\ c_\alpha s_\alpha \left(c_\theta - 1\right) & c_\alpha^2 + c_\theta s_\alpha^2 & s_\alpha s_\theta & s_\alpha \left(1 - c_\theta\right) L/\theta \\ -c_\alpha s_\theta & -s_\alpha s_\theta & c_\theta & s_\theta L/\theta + d \\ 0 & 0 & 0 & 1 \end{bmatrix}, \tag{5}
$$

where $s_\theta = \sin(\theta)$, $c_\theta = \cos(\theta)$, $s_\alpha = \sin(\alpha)$, $c_\alpha = \cos(\alpha)$, and parameters α, θ, L and d represent the bending direction, the bending angle, the length of the flexible joint part and the distance between the center of the actuation module and the proximal end of the flexible joint, respectively.

Coordinate frame 10 is attached to the center of the camera, which is positioned at the holder. The transformation matrix between coordinate frames 9 and 10 is as follows:

$$
{}^{9}\boldsymbol{T}_{10} = \begin{bmatrix} 1 & 0 & 0 & b_x \\ 0 & 1 & 0 & 0 \\ 0 & 0 & 1 & b_z \\ 0 & 0 & 0 & 1 \end{bmatrix}, \tag{6}
$$

where b_x and b_z denote the deviations between the distal end of the flexible joint and the camera along the X and Z axes. Consequently, the transformation matrix between coordinate frame 0 and coordinate frame 10 can be depicted as:

$$
{}^{0}\boldsymbol{T}_{10} = {}^{0}\boldsymbol{T}_{7}{}^{7}\boldsymbol{T}_{8}{}^{8}\boldsymbol{T}_{9}{}^{9}\boldsymbol{T}_{10}. \tag{7}
$$

Given that the endoscope possess a total of 5 DoFs. The mapping is as follows:

$$
{}^{8}\boldsymbol{\xi}_{\text{cam}} = \boldsymbol{J}_{\text{actuaor}}{}^{8}\boldsymbol{\xi}_{\text{act}}, \tag{8}
$$

$$
\boldsymbol{J}_{\text{acuator}} = \begin{bmatrix} 1 & 0 & e_{13} & e_{14} & e_{15} \\ 0 & 0 & 0 & e_{24} & e_{25} \\ 0 & 1 & e_{33} & e_{34} & e_{35} \\ 0 & 0 & 0 & e_{44} & e_{45} \\ 0 & 0 & 1 & e_{54} & e_{55} \\ 9 & 0 & 0 & e_{64} & 0 \end{bmatrix}, {}^{8}\boldsymbol{\xi}_{\text{act}} = \begin{bmatrix} {}^{8}v_{\text{act}x} \\ {}^{8}v_{\text{act}z} \\ \dot{\beta} \\ \dot{\alpha} \\ \dot{\theta} \end{bmatrix}, \tag{9}
$$

where ${}^{8}\boldsymbol{\xi}_{\text{cam}}$ denotes the linear and angular velocities of the camera in coordinate frame 8, ${}^{8}v_{\text{act}x}$ denotes the translational velocity of the actuation module along the X axis of coordinate frame 8, ${}^{8}v_{\text{act}z}$ denotes the translational velocity of the actuaiton module along the Z axis of coordinate frame 8, $\dot{\beta}$ denotes the rotational velocity of the actuaion module along the Y axis of coordinate frame 8, $\dot{\alpha}$ and $\dot{\theta}$ denote the velocities of bending direction and bending angel of the flexible joint, $e_{13} = d + b_z\cos(\theta) + L\sin(\theta)/\theta - b_x\cos(\alpha)\sin(\theta)$, $e_{14} = 2b_x\cos(\alpha)\sin(\alpha)(1-\cos(\theta)) - b_z\sin(\alpha)\sin(\theta) + L\sin(\alpha)(\cos(\theta)-1)/\theta$, $e_{15} = \cos(\alpha)(L\cos(\theta) - L + L\theta\sin(\theta) + b_z\theta^2\cos(\theta) - b_x\theta^2\cos(\alpha)\sin(\theta))/(\theta^2)$, $e_{24} = b_x\cos(2\alpha)(\cos(\theta)-1) + b_z\cos(\alpha)\sin(\theta) - L\cos(\alpha)(\cos(\theta)-1)/\theta$, $e_{25} = \sin(\alpha)(L\cos(\theta) - L + L\theta\sin(\theta) + b_Z\theta^2\cos(\theta) - b_x\theta^2\cos(\alpha)\sin(\theta))/\theta^2$, $e_{33} = L\cos(\alpha)(\cos(\theta)-1)/\theta - b_z\cos(\alpha)\sin(\theta) - b_x(\cos(\alpha)^2\cos(\theta) - \cos(\alpha)^2 + 1)$, $e_{34} = b_x\sin(\alpha)\sin(\theta)$, $e_{35} = L\cos(\theta)/\theta - b_z\sin(\theta) - b_x\cos(\alpha)\cos(\theta) - L\sin(\theta)/\theta^2$, $e_{44} = -\cos(\alpha)\sin(\theta)$, $e_{45} = -\sin(\alpha)$, $e_{54} = -\sin(\alpha)\sin(\theta)$, $e_{55} = \cos(\alpha)$, $e_{64} = 1 - \cos(\theta)$.

The five DoFs of the flexible endoscope are achieved through the 7 DoFs of the Franka Emika Panda robot and the 2 DoFs of the flexible joint. The mapping is as follows:

$$
{}^{8}\boldsymbol{\xi}_{\text{act}} = \boldsymbol{J}_2\boldsymbol{J}_1\dot{\boldsymbol{\theta}}, \tag{10}
$$

with

$$
\dot{\boldsymbol{\theta}} = \begin{bmatrix} \dot{\boldsymbol{\theta}}_{\text{robot}} \\ \dot{\alpha} \\ \dot{\theta} \end{bmatrix}, \boldsymbol{J}_1 = \begin{bmatrix} {}^{8}\boldsymbol{J}_{\text{robot}} & \boldsymbol{0}_{6\times2} \\ \boldsymbol{0}_{2\times7} & \boldsymbol{I}_{2\times2} \end{bmatrix},
$$

$$
\boldsymbol{J}_2 = \begin{bmatrix} 1 & 0 & 0 & 0 & 0 & 0 & 0 & 0 \\ 0 & 0 & 1 & 0 & 0 & 0 & 0 & 0 \\ 0 & 0 & 0 & 0 & 1 & 0 & 0 & 0 \\ 0 & 0 & 0 & 0 & 0 & 0 & 1 & 0 \\ 0 & 0 & 0 & 0 & 0 & 0 & 0 & 1 \end{bmatrix}, \tag{11}
$$

where ${}^{8}\boldsymbol{J}_{\text{robot}}$ represents the Jacobian matrix of the robot in coordinate frame 8, which can be gained by changing the coordinate frame of ${}^{0}\boldsymbol{J}_{\text{robot}}$, $\dot{\boldsymbol{\theta}} \in \mathrm{R}^{9\times1}$ denotes a joint

velocity vector compromising 7 DoFs of the Franka Emika Panda robot and 2 DoFs of the flexible joint.

B. Mapping Between Task Space and Image Space

The well-known pinhole camera model leads to the following kinematic equation [14]:

$$\dot{\boldsymbol{s}} = \boldsymbol{J}_{\text{image}}{}^{10}\boldsymbol{\xi}_{\text{cam}} \tag{12}$$

where

$$\boldsymbol{J}_{\text{image}} = \begin{bmatrix} -\frac{\bar{f}}{z} & 0 & \frac{\bar{u}}{z} & \frac{\bar{u}\bar{v}}{\bar{f}} & -\frac{\bar{f}^2+\bar{u}^2}{\bar{f}} & \bar{v} \\ 0 & \frac{\bar{f}}{z} & \frac{\bar{v}}{z} & \frac{\bar{f}^2+\bar{v}^2}{\bar{f}} & -\frac{\bar{u}\bar{v}}{\bar{f}} & -\bar{u} \end{bmatrix} \in \mathbb{R}^{2\times 6}, \tag{13}$$

where $\boldsymbol{J}_{\text{image}}$ is the image Jacobian that maps the instantaneous linear and angular velocities of the camera ${}^{10}\boldsymbol{\xi}_{\text{cam}} \in \mathbb{R}^6$ in the image coordinate frame, i.e., coordinate frame 10, to the image feature velocities $\dot{\boldsymbol{s}} = [\dot{u}, \dot{v}]$. In the image Jacobian, $\bar{u} = u - u_0$ and $\bar{v} = v - v_0$ with $s_0 = [u_0, v_0]^{\mathrm{T}}$ indicating the principle point of the image plane. Besides, $\bar{f} = \frac{f}{\rho}$ where f and ρ denote the focal length and the pixel width of each square pixel, respectively.

C. Magnetically Anchoring Constraints

For the MAGS flexible endoscope, it is anchored on the body cavity wall via the magnetic coupling formed by the EPM and IPM. The six DoFs of the actuation module in Cartesian space are constrained to two translational DoFs along the plane of the body cavity wall and a rotational DoF along the normal of the plane. The remaining three DoFs, including one translational DoF normal to the plane and two rotational DoFs along the other two axes in the plane, are not permitted, meaning that movements in these three DoFs should be zero. The constraints are given as follows:

$$\boldsymbol{0} = \boldsymbol{J}_3\boldsymbol{J}_1\dot{\boldsymbol{\theta}}, \tag{14}$$

with

$$\boldsymbol{J}_3 = \begin{bmatrix} 0 & 1 & 0 & 0 & 0 & 0 & 0 & 0 \\ 0 & 0 & 0 & 1 & 0 & 0 & 0 & 0 \\ 0 & 0 & 0 & 0 & 0 & 1 & 0 & 0 \end{bmatrix}. \tag{15}$$

D. Integrated Kinematics

Based on the above analysis, the following kinematic equations are derived to relate the image space and the joint space while considering magnetic anchoring constraints:

$$\boldsymbol{\varsigma} = \boldsymbol{J}_{\text{total}}\dot{\boldsymbol{\theta}} \tag{16}$$

with

$$\boldsymbol{J}_{\text{total}} = \begin{bmatrix} \boldsymbol{J}_{\text{image}}\boldsymbol{J}_4\boldsymbol{J}_{\text{actutor}}\boldsymbol{J}_2\boldsymbol{J}_1 \\ \boldsymbol{J}_3\boldsymbol{J}_1 \end{bmatrix}, \tag{17}$$

$$\boldsymbol{\varsigma} = \begin{bmatrix} \dot{\boldsymbol{s}} \\ \boldsymbol{0} \end{bmatrix}, \boldsymbol{J}_4 = \begin{bmatrix} {}^{10}\boldsymbol{T}_8 & \boldsymbol{0} \\ \boldsymbol{0} & {}^{10}\boldsymbol{T}_8 \end{bmatrix}. \tag{18}$$

where $\boldsymbol{\varsigma}$ is a vector with all equality constraints, $\boldsymbol{J}_4$ denotes the matrix that maps the instantaneous linear and angular velocities in coordinate frame 8 to coordinate frame 10.

IV. CONTROL SCHEME

This section formulates a visual servo control scheme for the presented endoscope. The control scheme is first established as a constrained quadratic programming formulation. Then, a zeroing neural network (ZNN) is implemented as the QP solver.

A. Control Scheme Formulation

Based on the kinematics analysis, a visual servo control scheme is formulated as the following constrained QP with physical limits considered:

$$\begin{aligned} \text{min.}: \quad & \dot{\boldsymbol{\theta}}^{\mathrm{T}}\boldsymbol{W}\dot{\boldsymbol{\theta}}/2 + \boldsymbol{q}^{\mathrm{T}}\dot{\boldsymbol{\theta}}, && (19) \\ \text{s.t.}: \quad & \boldsymbol{J}_{\text{total}}\dot{\boldsymbol{\theta}} = \boldsymbol{\varsigma}, && (20) \\ & \boldsymbol{\theta}^- \le \boldsymbol{\theta} \le \boldsymbol{\theta}^+, && (21) \\ & \dot{\boldsymbol{\theta}}^- \le \dot{\boldsymbol{\theta}} \le \dot{\boldsymbol{\theta}}^+, && (22) \end{aligned}$$

where the superscript $^{\mathrm{T}}$ denotes the transpose operator of a matrix or a vector, $\boldsymbol{W} \in \mathbb{R}^{n\times n}$ is a symmetric and positive definite weighting matrix and $\boldsymbol{q} \in \mathbb{R}^n$ is a vector for various task indices (e.g., repetitive motion planning), $\boldsymbol{\theta}$ and $\dot{\boldsymbol{\theta}}$ denote the joint positions and joint velocities of the endoscope, $\boldsymbol{\theta}^{\pm}$ and $\dot{\boldsymbol{\theta}}^{\pm}$ stand for the upper and lower limits of joint-position vector $\boldsymbol{x}$ and joint-velocity vector $\dot{\boldsymbol{\theta}}$, respectively.

By incorporating the joint-position and joint-velocity limits, the above QP can be reformulated as follows:

$$\begin{aligned} \text{min}: \quad & \boldsymbol{x}^{\mathrm{T}}\boldsymbol{W}\boldsymbol{x}/2 + \boldsymbol{q}^{\mathrm{T}}\boldsymbol{x}, && (23) \\ \text{s.t.}: \quad & \boldsymbol{A}\boldsymbol{x} = \boldsymbol{b}, && (24) \\ & \boldsymbol{x}^- \le \boldsymbol{x} \le \boldsymbol{x}^+, && (25) \end{aligned}$$

where $\boldsymbol{x} = \dot{\boldsymbol{\theta}}$, $\boldsymbol{A} = \boldsymbol{J}_{total}$, $\boldsymbol{b} = \boldsymbol{\varsigma}$, the joint-velocity limits and related functions are defined as follows:

$$x_i^- := \begin{cases} \dot{\theta}_i^-, & \text{if } \theta_i \in [c_i, \theta_i^+] \\ \dot{\theta}_i^-(1 - g_1(\theta_i)), & \text{if } \theta_i \in [\theta_i^-, c_i] \end{cases}, \tag{26}$$

$$x_i^+ := \begin{cases} \dot{\theta}_i^+, & \text{if } \theta_i \in [\theta_i^-, d_i] \\ \dot{\theta}_i^+(1 - g_2(\theta_i)), & \text{if } \theta_i \in [d_i, \theta^+] \end{cases}, \tag{27}$$

$$g_1(\theta_i) := \sin^2(0.5\pi \sin^2(0.5\pi(\theta_i - c_i)/e_i)), \tag{28}$$

$$g_2(\theta_i) := \sin^2(0.5\pi \sin^2(0.5\pi(\theta_i - d_i)/f_i)), \tag{29}$$

where $c_i = \alpha_1\theta_i^- + (1-\alpha_1)\theta_i^+$, $d_i = \alpha_2\theta_i^+ + (1-\alpha_2)\theta_i^-$, $e_i = \theta_i^- - c_i$ and $f_i = \theta_i^+ - d_i$; α_1 and α_2 are user-specific parameters and are set as a positive constant smaller than 1.

B. Visual Servo Controller

In order to avoid iteraions in the QP solving process, a ZNN model, i.e, the linear-variational-inequality based ZNN (LVI-ZNN) [15] is implemented to solve the QP problem (23)–(25):

$$\begin{aligned} \dot{\boldsymbol{y}} :=& (\boldsymbol{D} - \boldsymbol{D}\boldsymbol{M} - \boldsymbol{I})^{\dagger}(\boldsymbol{D}(\dot{\boldsymbol{M}}\boldsymbol{y} + \dot{\boldsymbol{z}}) \\ & - \gamma\boldsymbol{F}(\boldsymbol{P}_{\Omega}(\boldsymbol{v}) - \boldsymbol{y}) - (\boldsymbol{I} - \boldsymbol{D})\boldsymbol{L}), \end{aligned} \tag{30}$$

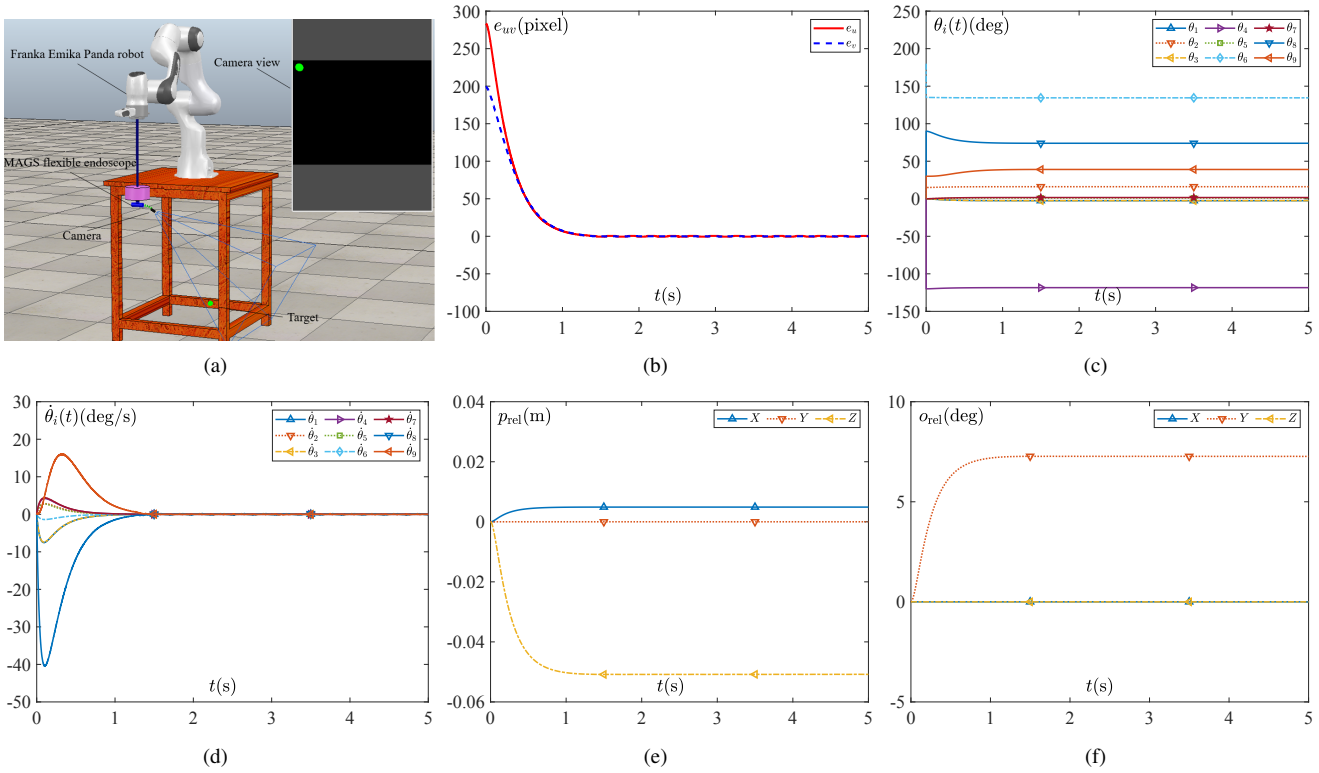

Fig. 2. Visual tracking results of the robotic endoscope following a static target controlled by the LVI-ZNN solver implemented in MATLAB for solving QP (23)-(25) with physical limit constraints and magnetically anchoring limits considered. (a) Initial state. (b) Distance from feature point to center of the image. (c) Resolved joint angles. (d) Resolved joint velocities. (e) Relative position between coordinate frame 8 and its initial state. (f) Relative orientation between coordinate frame 8 and its initial state.

with

$$\boldsymbol{y}=\begin{bmatrix}\boldsymbol{x}\\ \boldsymbol{u}\end{bmatrix}, \boldsymbol{M}=\begin{bmatrix}\boldsymbol{W} & -\boldsymbol{A}^{\mathrm{T}}\\ \boldsymbol{A} & \boldsymbol{0}\end{bmatrix}, \boldsymbol{z}=\begin{bmatrix}\boldsymbol{q}\\ -\boldsymbol{b}\end{bmatrix}, \tag{31}$$

$$\boldsymbol{v}:=\boldsymbol{y}-\boldsymbol{M}\boldsymbol{y}-\boldsymbol{z}, \boldsymbol{P}_{\Omega}(v_i):=\begin{cases} y_i^+, & \text{if } v_i>y_i^+\\ v_i, & \text{if } y_i^+\le v_i\le y_i^+\\ y_i^-, & \text{if } v_i<y_i^- \end{cases}, \tag{32}$$

$$d_i:=\begin{cases} 0, & \text{if } v_i>y_i^+\\ 0, & \text{if } v_i=y_i^+ \text{ and } \dot{v}_i>\dot{y}_i^+\\ \{0,1\}, & v_i=y_i^+ \text{ and } \dot{v}_i=\dot{y}_i^+\\ 1, & \text{if } v_i=y_i^+\neq\dot{y}_i^-\\ & \text{and } \dot{v}_i<y_i^+\\ 1, & \text{if } v_i=y_i^+=y_i^-\\ & \text{and } \dot{y}_i^-<\dot{v}_i<\dot{y}_i^+\\ 1, & \text{if } y_i^-<v_i<y_i^+\\ 1, & \text{if } v_i=y_i^-\neq\dot{y}_i^+\\ & \text{and } \dot{v}_i>\dot{y}_i^-\\ \{0,1\}, & \text{if } v_i=y_i^- \text{ and } \dot{v}_i=\dot{y}_i^-\\ 0, & \text{if } v_i=y_i^- \text{ and } \dot{v}_i<\dot{y}_i^-\\ 0, & \text{if } v_i<y_i^- \end{cases}, \tag{33}$$

$$l_i:=\begin{cases} \dot{y}_i^+, & \text{if } v_i\ge y_i^+\\ 0, & \text{if } y_i^-<v_i<y_i^+\\ \dot{y}_i^-, & \text{if } v_i\le y_i^- \end{cases}, \tag{34}$$

where $\boldsymbol{y}$ is the decision variable, $\boldsymbol{M}$ is an augmented matrix, $\boldsymbol{z}$ is an augmented vector, $\boldsymbol{P}_{\Omega}(\cdot)$ represents a piecewise linear projection operator which projects the vector $\boldsymbol{v}$ between the upper limit $\boldsymbol{y}^+$ and lower limit $\boldsymbol{y}^-$ of $\boldsymbol{y}$, γ is a user-specified positive constant for scaling the speed of convergence, the superscript † denotes the pseudoinverse of a matrix, $\boldsymbol{F}(\cdot)$ is an activation function array of which each element is a monotonically non-decreasing odd function $f(\cdot)$, $\boldsymbol{I}$ is an identity matrix, $\boldsymbol{D}=\mathrm{diag}([D_1,\cdots,D_i,\cdots,D_n]^{\mathrm{T}})$, $\boldsymbol{L}=\mathrm{diag}([l_1,\cdots,l_i,\cdots,l_n]^{\mathrm{T}})$.

V. SIMULATIVE VALIDATIONS

To verify the effectiveness of visual servo control of the MAGS flexible endoscope, the LVI-ZNN is applied to achieve visual servo control, as shown in Fig. 2(a) and Fig. 3(a), in a robot simulator named CoppeliaSim [16]. The simulator is interfaced with MATLAB R2021a installed on a personal computer with an Intel Core i7-10750H 2.60-GHz CPU, 16-GB RAM, and a Windows 10 operating system. For the endoscope system, the initial joint angles are set as $\boldsymbol{\theta}(0)=[0,15,0,-120,0,135,0,90,30]^{\mathrm{T}}$deg; the upper and lower joint-angle limits are set as $\boldsymbol{\theta}^+=[166,101,166,-4,166,215,166,180,90]^{\mathrm{T}}$ deg and $\boldsymbol{\theta}^-=[-166,-101,-166,-176,-166,-1,-166,-180,-90]^{\mathrm{T}}$

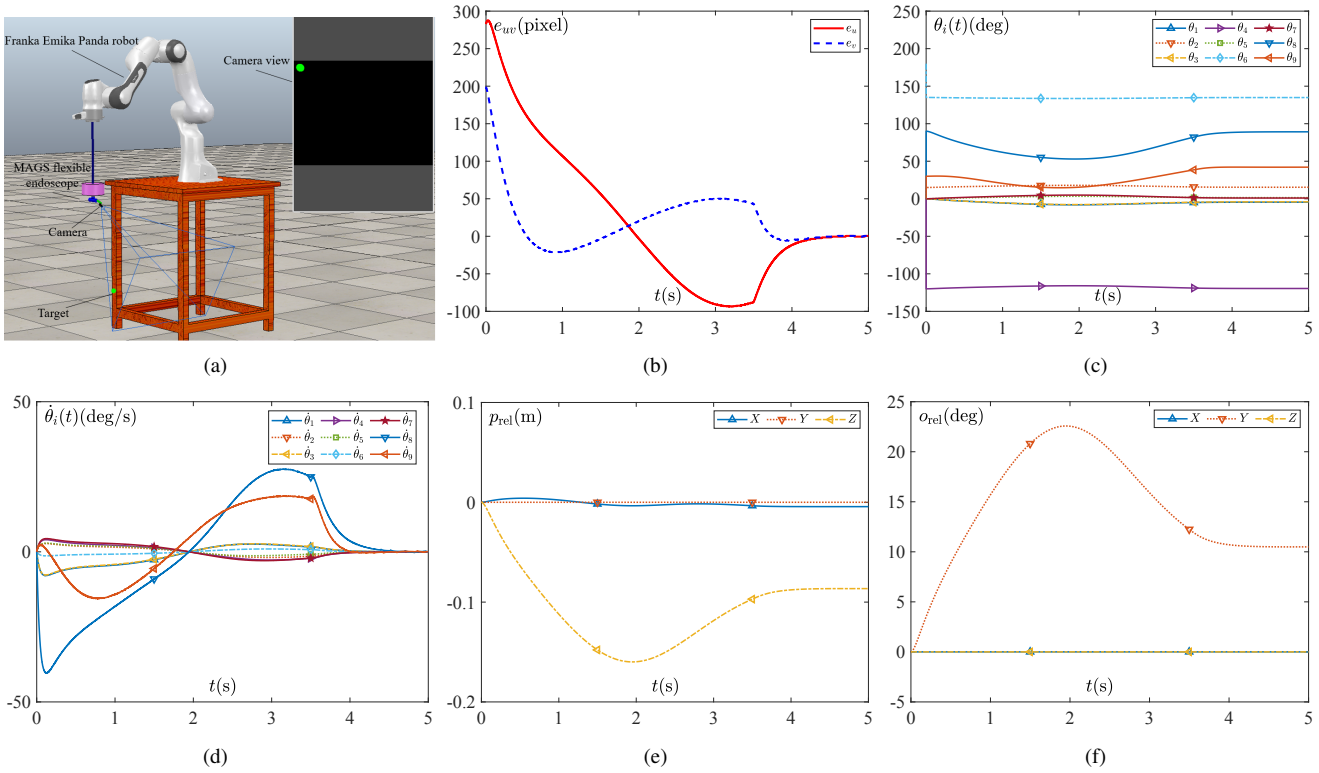

Fig. 3. Visual tracking results of the robotic endoscope following a dynamic target controlled by the LVI-ZNN solver implemented in MATLAB for solving QP (23)-(25) with physical limit constraints and magnetically anchoring limits considered. (a) Initial state. (b) Distance from feature point to center of the image. (c) Resolved joint angles. (d) Resolved joint velocities. (e) Relative position between coordinate frame 8 and its initial state. (f) Relative orientation between coordinate frame 8 and its initial state.

deg; the initial upper and lower joint-velocity limits are set as $\dot{\boldsymbol{\theta}}^{+} = [150, 150, 150, 150, 150, 180, 180, 360, 360]^{\mathrm{T}}$ deg/s and $\dot{\boldsymbol{\theta}}^{-} = -\dot{\boldsymbol{\theta}}^{+}$. The task duration is $T = 5$ s with sampling gap $\tau = 0.001$ s, and $\gamma = 30$. The weighting matrix is set as $\boldsymbol{W} = \mathrm{diag}([1, 1, 1, 1, 1, 1, 1, 0.05, 0.005]^{\mathrm{T}})$, the index vector is set as $\boldsymbol{q} = \boldsymbol{0}$. The endoscope is assigned to carry out two tasks: The first is to track a static target at the position $[0.75; 0.5; 0.33]$; the second is to track a target of which the desired path is designed as $[0.75 + 0.2\sin(t); 0.5; 0.33 + 0.2\sin(t)]$ with $t \in [0, 3.5]$ s.

As depicted in Fig. 2(a) and Fig. 3(a), the targets are situated at the top left corner of the camera view. Subsequently, as illustrated in Fig. 2(b) and Fig. 3(b), the static and dynamic targets are both ultimately positioned at the center of the camera view, indicating successful achievement of visual servo control for following static and dynamic targets. Though some fluctuations can be found in Fig. 3(b) due to the movement of the target. Fig. 2(c) and Fig. 3(c) reveal that all joint angles, including those of the robot's joints, bending angle, and bending direction, remain within their respective limits throughout the tasks. Additionally, joint velocities displayed in Fig. 2(d) and Fig. 3(d) indicate that all joint velocities are within acceptable limits. Fig. 2(e) and Fig. 2(e) demonstrate that the relative positions between coordinate frame 8 and its initial state along the Y axis are both approximately zero. Furthermore, Fig. 2(f) and Fig. 3(f) indicate that the relative orientation between coordinate frame 8 and its initial state along the X axis and Z axis is approximately zero. The results in Fig. 2(e)-(f) and Fig. 3(e)-(f) have confirmed that the magnetically anchoring constraints are both well satisfied when following a static or a dynamic target.

VI. Conclusion

This paper presents a conceptual magnetically anchored and guided flexible endoscope. The kinematic modeling and the control scheme of the endoscope have been formulated as a QP-based framework by introducing magnetically anchoring constraints as equality constraints, where the joint velocities can be resolved given the desired task velocities in a one-step way. Simulative validations have been conducted to follow a static and a dynamic target by using a ZNN as the visual servo controller, verifying the effectiveness of the visual servo control of the presented endoscope. While this study has provided the theoretical insights and simulative validations of the endoscope design, future research should prioritize the fabrication and testing of a physical prototype of the endoscope.

References

[1] T. Robinson and G. Stiegmann, "Minimally invasive surgery," *Endoscopy*, vol. 36, no. 01, pp. 48–51, 2004.

[2] D. Canes, M. M. Desai, M. Aron, G.-P. Haber, R. K. Goel, R. J. Stein, J. H. Kaouk, and I. S. Gill, "Transumbilical single-port surgery: evolution and current status," *Eur. Urol.*, vol. 54, no. 5, pp. 1020–1030, 2008.

[3] S. Park, R. A. Bergs, R. Eberhart, L. Baker, R. Fernandez, and J. A. Cadeddu, "Trocar-less instrumentation for laparoscopy: magnetic positioning of intra-abdominal camera and retractor," *Ann. Surg.*, vol. 245, no. 3, p. 379, 2007.

[4] I. S. Zeltser, R. Bergs, R. Fernandez, L. Baker, R. Eberhart, and J. A. Cadeddu, "Single trocar laparoscopic nephrectomy using magnetic anchoring and guidance system in the porcine model," *J. Urol.*, vol. 178, no. 1, pp. 288–291, 2007.

[5] J. Cadeddu, R. Fernandez, M. Desai, R. Bergs, C. Tracy, S.-J. Tang, P. Rao, M. Desai, and D. Scott, "Novel magnetically guided intra-abdominal camera to facilitate laparoendoscopic single-site surgery: initial human experience," *Surg. Endosc.*, vol. 23, pp. 1894–1899, 2009.

[6] W. Li, T. Cheng, M. Ye, C. S. H. Ng, P. W. Y. Chiu, and Z. Li, "Kinematic modeling and visual servo control of a soft-bodied magnetic anchored and guided endoscope," *IEEE/ASME Trans. Mechatron.*, vol. 25, no. 3, pp. 1531–1542, 2020.

[7] T. Cheng, W. Li, W. Y. Ng, Y. Huang, J. Li, C. S. H. Ng, P. W. Y. Chiu, and Z. Li, "Deep learning assisted robotic magnetic anchored and guided endoscope for real-time instrument tracking," *IEEE Robot. Autom. Lett.*, vol. 6, no. 2, pp. 3979–3986, 2021.

[8] R. J. Webster, J. M. Romano, and N. J. Cowan, "Mechanics of precurved-tube continuum robots," *IEEE Trans. Robot.*, vol. 25, no. 1, pp. 67–78, 2008.

[9] Z. Li, H. Ren, P. W. Y. Chiu, R. Du, and H. Yu, "A novel constrained wire-driven flexible mechanism and its kinematic analysis," *Mech. Mach. Theory*, vol. 95, pp. 59–75, 2016.

[10] D. Ji, T. H. Kang, S. Shim, S. Lee, and J. Hong, "Wire-driven flexible manipulator with constrained spherical joints for minimally invasive surgery," *Int. J. Comput. Assist. Radiol. Surg.*, vol. 14, pp. 1365–1377, 2019.

[11] X. Zhang, W. Li, P. W. Y. Chiu, and Z. Li, "A novel flexible robotic endoscope with constrained tendon-driven continuum mechanism," *IEEE Robot. Autom. Lett.*, vol. 5, no. 2, pp. 1366–1372, 2020.

[12] B. Siciliano, O. Khatib, and T. Kröger, *Springer Handbook of Robotics*. Berlin/Heidelberg, Germany: Springer, 2008.

[13] Z. Li, M. Zin Oo, V. Nalam, V. Duc Thang, H. Ren, T. Kofidis, and H. Yu, "Design of a novel flexible endoscope–cardioscope," *J. Mech. Robot.*, vol. 8, no. 5, p. 051014, 2016.

[14] S. Hutchinson, G. D. Hager, and P. I. Corke, "A tutorial on visual servo control," *IEEE Trans. Robot. Autom.*, vol. 12, no. 5, pp. 651–670, 1996.

[15] Y. Yang, W. Li, B. Song, Y. Zou, and Y. Pan, "Enhanced fault tolerant kinematic control of redundant robots with linear-variational-inequality based zeroing neural network," *Eng. Appl. Artif. Intell.*, vol. 133, p. 108068, 2024.

[16] E. Rohmer, S. P. Singh, and M. Freese, "V-REP: A versatile and scalable robot simulation framework," in *Proc. IEEE Int. Conf. Intell. Robot. Syst.*, 2013, pp. 1321–1326.